

Machine-Learning Insights on Entanglement-trainability Correlation of Parameterized Quantum Circuits

Shikun Zhang,¹ Yang Zhou,^{1,*} Zheng Qin,¹ Rui Li,¹ Chunxiao Du,¹ Zhisong Xiao,^{1,2} and Yongyou Zhang^{3,†}

¹*School of Physics, Beihang University, Beijing 100191, China*

²*School of Instrument Science and Opto-Electronics Engineering,*

Beijing Information Science and Technology University, Beijing 100192, China

³*School of Physics, Beijing Institute of Technology, Beijing 100081, China*

Variational quantum algorithms (VQAs) have emerged as the leading strategy to obtain quantum advantage on the current noisy intermediate-scale devices. However, their entanglement-trainability correlation, as the major reason for the barren plateau (BP) phenomenon, poses a challenge to their applications. In this Letter, we suggest a gate-to-tensor (GTT) encoding method for parameterized quantum circuits (PQCs), with which two long short-term memory networks (L-G networks) are trained to predict both entanglement and trainability. The remarkable capabilities of the L-G networks afford a statistical way to delve into the entanglement-trainability correlation of PQCs within a dataset encompassing millions of instances. This machine-learning-driven method first confirms that the more entanglement, the more possible the BP problem. Then, we observe that there still exist PQCs with both high entanglement and high trainability. Furthermore, the trained L-G networks result in an impressive increase in time efficiency by about one million times when constructing a PQC with specific entanglement and trainability, demonstrating their practical applications in VQAs.

Introduction.—In the current noisy intermediate-scale quantum era [1, 2], variational quantum algorithms (VQAs) garner wide interest due to their low consumption of quantum resources and noisy friendliness [3, 4]. Reported VQAs include variational quantum eigensolver [5–11], quantum approximate optimization algorithm [12–14], variational quantum machine learning [15–17] and so on. These VQAs implement parameterized quantum circuits (PQCs) on a quantum computer. PQCs primarily determine the computational performance of VQAs [18, 19]. Given that entanglement is the foundation of the unique characteristics and advantages of quantum systems over classical ones [18, 20–25], it naturally serves as a primary guiding principle in constructing PQCs. However, the heuristic nature of VQAs results in a lack of guaranteed performance of PQCs [23]. Significant researches on VQAs’ performance have been reported [23, 24, 26–36]. On one hand, PQCs with high entanglement were required to capture non-trivial quantum correlations or ground states of interested quantum systems [37–40]. On the other hand, the improper amount of entanglement may hinder the performance of VQAs [18, 41]. A markable question is the barren plateau (BP) phenomenon [25, 42, 43].

When BP occurs, the gradients of the cost functions in VQAs vanish exponentially with the system size [29, 44–47]. This implies an exponential number of measurement shots are needed to resolve and determine the cost-minimizing direction. Such exponential complexity would undermine the quantum advantages of VQAs [4]. Recently, Ortiz Marrero et al. showed that entanglement between visible and hidden units in a Quantum Neural

Network reduces trainability [43]. Patti et al. implicated random entanglement as a source of barren plateaus and characterized them in terms of many-body entanglement dynamics [25]. These existing studies, based on analytical theoretical derivations, only provide a rudimentary correlation between entanglement and trainability. The more fundamental and general relationship between them remains elusive. The major difficulty relies on the fact that the number of possible PQCs is frighteningly huge and the evaluation of entangling capability and trainability for a PQC presents significant challenges in practice. Neural networks show remarkable potential in addressing these complex issues. Current research has shown their applications in performing quantum architecture searchers [48], constructing generative quantum eigensolvers [49], synthesizing quantum circuits [50] and predicting PQCs’ expressibility [51, 52]. Utilizing advancements in machine learning has been proven helpful in overcoming persistent challenges in quantum algorithms.

In this Letter, we propose a machine-learning method to efficiently evaluate entangling capability and trainability based on which the general entanglement-trainability correlation of PQCs is explored. An innovative scheme is suggested to encode PQCs into tensors, referred to as the gate-to-tensor (GTT) encoding. Using the GTT code as input, two long short-term memory (LSTM) networks, dubbed the L-G network, are trained to predict both entanglement and trainability, as illustrated in Fig. 1. The L-G network offers at least three merits: (i) the one-gate-to-one-tensor strategy lets the PQCs with the same numbers of quantum gates and qubits possess the mapping tensors with identical size; (ii) the GTT encoding can effectively capture the mutual control information among qubits; (iii) the temporal nature of the LSTM block enables it to simulate the information flow within PQCs. The remarkable capabilities of the L-G networks

* Contact author: yangzhou9103@buaa.edu.cn

† Contact author: yyzhang@bit.edu.cn

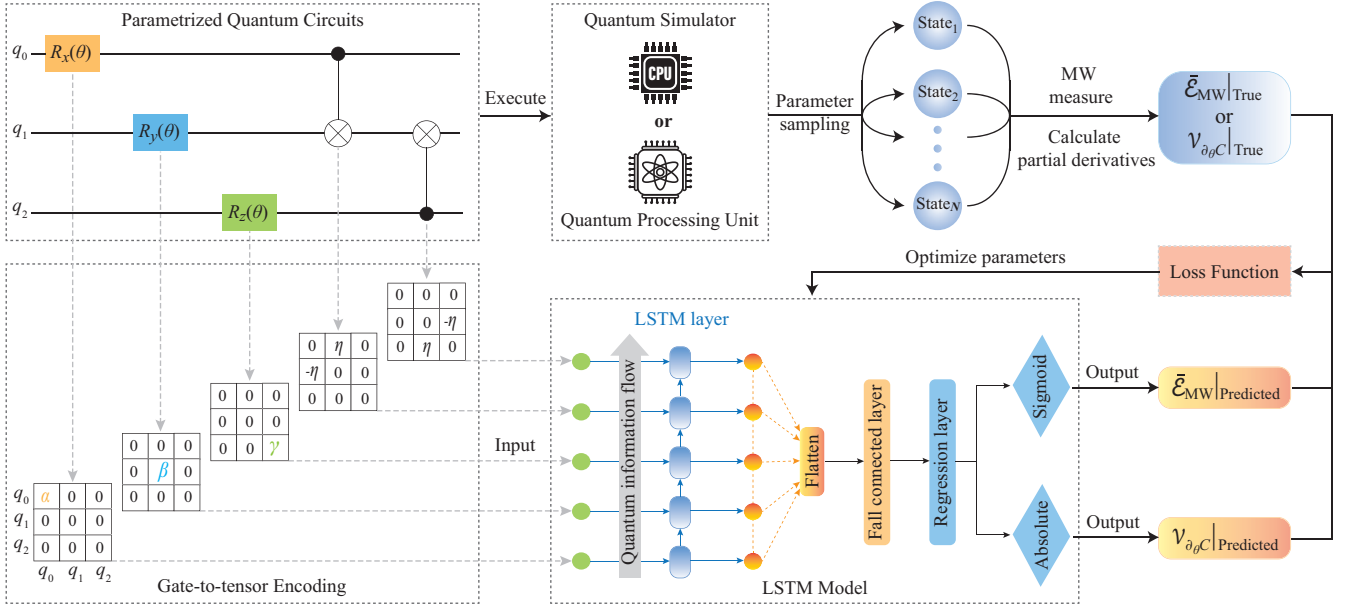


FIG. 1. The L-G networks for predicting the entangling capability ($\bar{\mathcal{E}}_{\text{MW}}$) and trainability ($\mathcal{V}_{\partial_\theta C}$) of PQCs. The true $\bar{\mathcal{E}}_{\text{MW}}$ or $\mathcal{V}_{\partial_\theta C}$ of PQCs is determined by sampling the parameter space multiple times and executing PQCs on a quantum simulator or quantum processing unit. We utilize the proposed gate-to-tensor method to encode PQCs into a tensor. This tensor is then fed into the LSTM model across different time steps to predict the $\bar{\mathcal{E}}_{\text{MW}}$ and $\mathcal{V}_{\partial_\theta C}$.

afford a statistical way to delve into the entanglement-trainability correlation within a dataset encompassing millions of instances. We confirm the negative correlation between trainability and entanglement, and demonstrate that the BP phenomenon is statistical, enabling it to be circumvented in computational tasks, even when addressing high levels of entanglement. Furthermore, statistical properties of the three topological parameters of PQCs, i.e., the ratio of C-Not gates, the circuit connectivity density, and the average adjacency matrix, are demonstrated on the 2D space of the entanglement and trainability. Finally, by utilizing the statistical properties of the three topological parameters and the trained L-G networks, we develop an algorithm for constructing PQCs with specific entanglement and trainability. This algorithm leads to a remarkable increase in time efficiency, approximately one million times, demonstrating its practical applications in the field of VQAs.

Method.—PQCs’ entangling capability is typically quantified by the average Meyer-Wallach entanglement measure [37] while BPs are usually quantified in terms of unitary t -designs [53–55], with trainability dynamics depending solely on the variance of the partial derivatives. The average Meyer-Wallach entanglement ($\bar{\mathcal{E}}_{\text{MW}}$) [37] is defined as

$$\bar{\mathcal{E}}_{\text{MW}} \equiv \frac{1}{|S|} \sum_{\theta_i \in S} \text{MW}(|\psi_{\theta_i}\rangle), \quad (1)$$

where $S = \{\theta_i\}$ represents the sets of sampled parameter vectors in the parameter space of a PQC and $|S|$ represents the number of sampled parameter vectors. The

variance of the gradient of the cost function ($\mathcal{V}_{\partial_\theta C}$) [42] can be expressed as,

$$\mathcal{V}_{\partial_\theta C} = \langle (i\langle 0|U_{\mathcal{R}}^\dagger[V_k, U_{\mathcal{L}}^\dagger H U_{\mathcal{L}}]U_{\mathcal{R}}|0\rangle)^2 \rangle, \quad (2)$$

where $U_{\mathcal{L}}$ and $U_{\mathcal{R}}$ represent a bipartite cut of a PQC, $V_k = \bigotimes_{j=1}^n \sigma_j$ is a Hermitian operator. (See the Supplemental Material [56] for detailed derivation and explanation of Eq. (1) and (2)). A preliminary draft for computing $\bar{\mathcal{E}}_{\text{MW}}$ and $\mathcal{V}_{\partial_\theta C}$ is illustrated in the first row of Fig. 1. The convergence of $\bar{\mathcal{E}}_{\text{MW}}$ ($\mathcal{V}_{\partial_\theta C}$) typically necessitates parameter sampling on the order of twenty thousand (one thousand) of samples; consequently, their computation demands substantial computational resources. (See the Supplemental Material [56] for details of discussion). It is this observation that motivates us to develop a neural network that maps the functional relationship between the PQC structure and either $\bar{\mathcal{E}}_{\text{MW}}$ or $\mathcal{V}_{\partial_\theta C}$.

Encoding PQCs as tensors for machine learning models is the fundamental technology. This point leads to the image encoding strategy that transforms a PQC into a multi-channel image encoding (IE) [48], while it overlooks the mutual control information among qubits. The proposed GTT encoding transforms PQCs into tensors of dimension $L \times N \times N$, where L and N are the numbers of quantum gates and qubits, respectively. The GTT encoding scheme can accurately capture all structural information of PQCs and simultaneously be compatible with the data processing characteristics of machine learning models. These advantages enable it to outperform the IE of PQCs [48]. The outperformance of the L-G network for predicting $\bar{\mathcal{E}}_{\text{MW}}$ has been proven through comparison

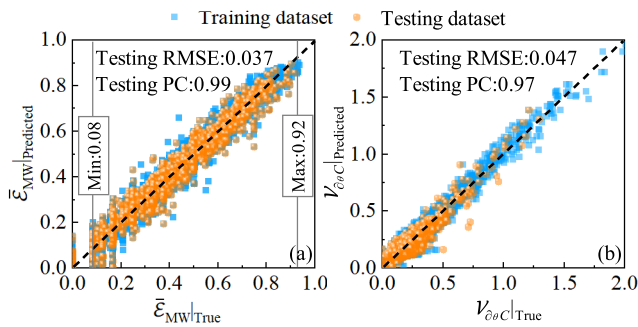


FIG. 2. Confusion scatters for predicted and true values of $\bar{\mathcal{E}}_{\text{MW}}$ (a) and $\mathcal{V}_{\partial_\theta C}$ (b) on both training and testing datasets.

with the IE [48]. (See the Supplemental Material [56] for a detailed comparison between IE and GTT). Four types of quantum gates, i.e., $R_x(\theta)$, $R_y(\theta)$, $R_z(\theta)$, and C-Not, are considered in this work. Rotating gates have one non-zero element in their tensors, while the C-Not gate has two. If $R_x(\theta)$ [$R_y(\theta)$ or $R_z(\theta)$] rotates the n th qubit, the non-zero element is the n th diagonal one, set to α [β or γ]. If C-Not gate represents the control of the n th qubit on the n' th, the two non-zero elements are the nn' th and $n'n$ th, set to η and $-\eta$, respectively. An example of the GTT encoding with $L = 5$ and $N = 3$ is shown on the left of Fig. 1.

The workflow of the L-G network for predicting either $\bar{\mathcal{E}}_{\text{MW}}$ or $\mathcal{V}_{\partial_\theta C}$ is shown in the second row of Fig. 1, the flatten layer, full connected layer, and regression layer are added after the LSTM block. (See the Supplemental Material [56] for details of network structure.) When training L-G networks, all PQCs are generated by randomly specifying the gate type and related qubits thirty times, that is, each PQC has thirty gates. This procedure enables PQCs' structures to possess sufficient diversity. In training, the twenty thousand PQCs are divided into training and testing datasets in a ratio of 9 : 1.

Performance.—The performance of the GTT encoding depends on the encoding values of α , β , γ , and η . In training, they are taken as the hyperparameters of the L-G network and it is available to take $\alpha = 1$, $\beta = 2$, $\gamma = 3$, and $\eta = 4$ after some experiments. Additionally, the Adam optimizer and batch size of 1000 are employed to enhance computational efficiency, training stability, and convergence. Since the Huber loss [57] combines the benefits of mean squared error and mean absolute error, it is always adopted in our work. The model's resilience to data and hyper-parameter variations are ensured by implementing multiple experiments and retaining the best-performing model, which can also prevent overfitting and ensure effectiveness in real-world scenarios.

The detailed performance of the trained L-G networks for $\bar{\mathcal{E}}_{\text{MW}}$ and $\mathcal{V}_{\partial_\theta C}$ are shown in Figs. 2. To intuitively showcase their predictive capabilities, confusion scatters are plotted on both training and testing datasets. In Fig. 2(a) [Fig. 2(b)], the horizontal axis depicts the true

values of $\bar{\mathcal{E}}_{\text{MW}}$ [$\mathcal{V}_{\partial_\theta C}$], whereas the vertical axis displays the predicted ones. The dashed regression lines in Figs. 2(a) and 2(b) denote the ideal alignment between the predicted and true values. The confusion scatters reveal that the predicted $\bar{\mathcal{E}}_{\text{MW}}$ and $\mathcal{V}_{\partial_\theta C}$ closely align with their true counterparts. Their small root mean square errors (RMSEs) of 0.037 and 0.047 on the testing dataset further substantiate this claim. The Pearson correlation coefficients (PCs) for both $\bar{\mathcal{E}}_{\text{MW}}$ and $\mathcal{V}_{\partial_\theta C}$ are also high, as evidenced by their values of 0.99 and 0.97. Compared to the reported neural networks, the L-G networks exhibit superior performance [51, 52]. The excellent coincidence of confusion scatters on training and testing datasets suggests the absence of overfitting.

The L-G network for $\bar{\mathcal{E}}_{\text{MW}}$ can be further refined by taking into account the following observations. Firstly, the entanglements of PQCs originate from the C-Not gates; hence, the equation $\bar{\mathcal{E}}_{\text{MW}} = 0$ implies the absence of C-Not gates in PQCs, as seen in the leftmost one-column dots in Fig. 2(a). Secondly, $\bar{\mathcal{E}}_{\text{MW}}$ is a statistical measure. Consequently, $\bar{\mathcal{E}}_{\text{MW}}$ should have a non-zero minimum and a maximum as long as PQCs incorporate C-Not gates, as indicated by $\bar{\mathcal{E}}_{\text{MW}}|_{\text{min}} \simeq 0.08$ and $\bar{\mathcal{E}}_{\text{MW}}|_{\text{max}} \simeq 0.92$ in Fig. 2(a). (See the Supplemental Material [56] for details of explanation.) They prompt us to discard zero- $\bar{\mathcal{E}}_{\text{MW}}$ PQCs. Note that the aforementioned observations are not applicable to $\mathcal{V}_{\partial_\theta C}$. In practice, the L-G network without these observations still has acceptable performance and therefore, they are ignored when training the L-G network for $\bar{\mathcal{E}}_{\text{MW}}$. However, when using the trained L-G network to analyze the entanglement-trainability correlation, those PQCs with $\bar{\mathcal{E}}_{\text{MW}} < \bar{\mathcal{E}}_{\text{MW}}|_{\text{min}}$ or $\bar{\mathcal{E}}_{\text{MW}} > \bar{\mathcal{E}}_{\text{MW}}|_{\text{max}}$ are neglected.

Results.—To analyze the relationship between $\bar{\mathcal{E}}_{\text{MW}}$ and $\mathcal{V}_{\partial_\theta C}$, we initially generate three million PQCs and then predict their $\bar{\mathcal{E}}_{\text{MW}}$ and $\mathcal{V}_{\partial_\theta C}$ using the trained L-G networks. The main observations are listed below.

Observation 1. *A negative correlation exists between $\bar{\mathcal{E}}_{\text{MW}}$ and $\mathcal{V}_{\partial_\theta C}$, and the BP is statistical, enabling its circumvention in computational tasks.*

Figure 3(a) illustrates the probability distribution of the three million PQCs within the 2D space of $\bar{\mathcal{E}}_{\text{MW}}$ and $\mathcal{V}_{\partial_\theta C}$. The contour lines exhibit a downward shift as $\bar{\mathcal{E}}_{\text{MW}}$ increases, except the region where $\bar{\mathcal{E}}_{\text{MW}} \lesssim 0.08$, suggesting that trainability exhibits a decreasing trend when PQC's entanglement increases. This negative correlation between trainability and entanglement is further confirmed by observing the variation in the mean (or median) value of $\mathcal{V}_{\partial_\theta C}$ with respect to the entanglement, as depicted in Fig. 3(b). Such a negative correlation behavior aligns with the earlier reports [25]. The blue shadow in Fig. 3(b) represents the variance of $\mathcal{V}_{\partial_\theta C}$.

In Fig. 3(a), the number of PQCs within each identical interval of $\bar{\mathcal{E}}_{\text{MW}}$ differs. To counteract this effect, we randomly generate ten thousands of PQCs for three cases with $\bar{\mathcal{E}}_{\text{MW}} = 0.2, 0.5, \text{ and } 0.8$, respectively. Their probability distributions concerning $\mathcal{V}_{\partial_\theta C}$ are depicted in Fig. 3(c). The peak of the distribution shifts toward the

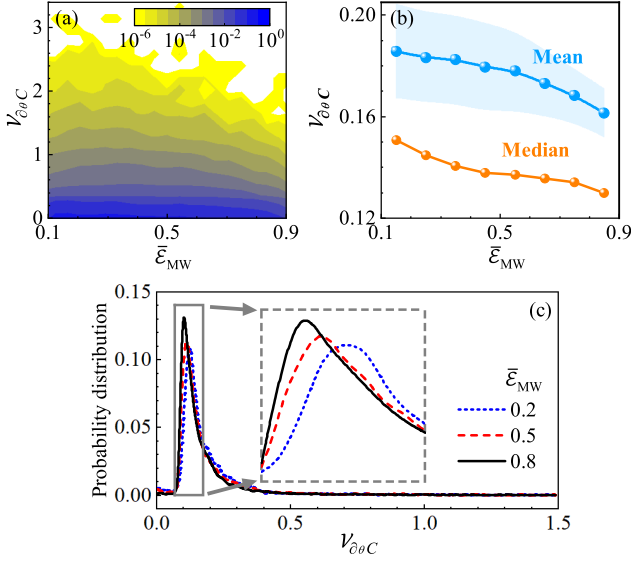


FIG. 3. (a) The probability distribution of the three million PQCs within the 2D space of $\mathcal{V}_{\partial\theta C}$ and $\bar{\mathcal{E}}_{MW}$. (b) The mean, variance, and median of $\mathcal{V}_{\partial\theta C}$ corresponding to each interval of discretized $\bar{\mathcal{E}}_{MW}$. (c) The probability distribution of $\mathcal{V}_{\partial\theta C}$ corresponding to $\bar{\mathcal{E}}_{MW}$ of 0.2, 0.5 and 0.8, respectively.

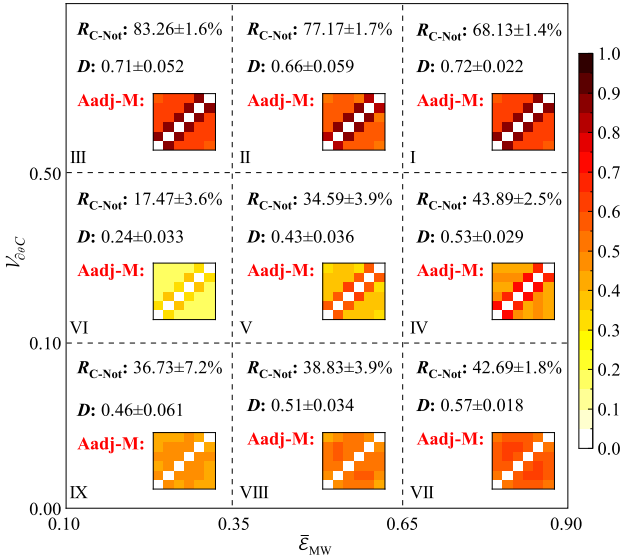


FIG. 4. Nine squares divided based on $\bar{\mathcal{E}}_{MW}$ and $\mathcal{V}_{\partial\theta C}$. In each square, the ratio of C-Not gates (R_{C-Not}) was calculated. PQCs were mapped onto undirected graphs, the circuit connectivity density (D) and the average adjacency matrix (Aadj-M) were calculated for each square.

left as $\bar{\mathcal{E}}_{MW}$ rises from 0.2 to 0.8. This also underscores the negative correlation between trainability and entanglement, implying an increase in the PQC's entanglement correlating with a higher likelihood of encountering the BP phenomenon.

The aforementioned analysis simultaneously reveals

that the negative correlation between trainability and entanglement is a statistical inference. Thus, it might be possible to construct the PQC with any values of $\bar{\mathcal{E}}_{MW}$ and $\mathcal{V}_{\partial\theta C}$. To elucidate this, we partition the 2D space of $\bar{\mathcal{E}}_{MW}$ and $\mathcal{V}_{\partial\theta C}$ into nine squares, see Fig. 4. By employing the trained L-G networks, we statistically determine three topological parameters of PQCs within each square: the ratio of C-Not gates (R_{C-Not}), the circuit connectivity density (D), and the average adjacency matrix (Aadj-M). R_{C-Not} and D are defined as follows,

$$R_{C-Not} = N_{C-Not}/L, \quad D = 2N_{Edge}/[N(N-1)], \quad (3)$$

where N_{C-Not} represents the number of C-Not gates and N_{Edge} corresponds to the number of edges in an undirected graph mapped from a PQC [24]. The adjacency matrix is a square matrix representing the connections between nodes in a graph. In this work, Aadj-M is obtained by calculating the average adjacency matrix of PQCs, quantifying the occurrence probability of each qubit pair defined by C-Not gates. Although the precise values of the topological parameters marginally depend on how the nine squares are partitioned, the subsequent findings remain consistent when viewed from a statistical standpoint.

Observation 2. *Increasing R_{C-Not} can appropriately lead to higher values of both $\bar{\mathcal{E}}_{MW}$ and $\mathcal{V}_{\partial\theta C}$; however, caution should be exercised to avoid exceeding the threshold, which is approximately 68%.*

Regarding the low- and moderate-trainability squares (two bottom rows), R_{C-Not} demonstrates a positive correlation with $\bar{\mathcal{E}}_{MW}$; however, in the high-trainability squares (top row), R_{C-Not} exhibits a negative correlation with $\bar{\mathcal{E}}_{MW}$. Furthermore, for low- and moderate-entanglement squares (left two columns), R_{C-Not} attains its smallest values when $\mathcal{V}_{\partial\theta C}$ is moderate; whereas, in the high-entanglement squares (right column), R_{C-Not} reaches its maximum value when $\mathcal{V}_{\partial\theta C}$ is high. Consequently, it can be inferred the Observation 2. The top-row squares reveal such threshold value for R_{C-Not} , approximately 68%, see the top-right square.

Observation 3. *Increasing D can significantly enhance $\bar{\mathcal{E}}_{MW}$, but this effect weakens at high $\mathcal{V}_{\partial\theta C}$. In circuits with high $\mathcal{V}_{\partial\theta C}$, C-Not gates tend to favor nearest-neighbor connections, while in circuits with low $\mathcal{V}_{\partial\theta C}$, they tend to be arbitrarily connected.*

Concerning the circuit connectivity density D , Fig. 4 illustrates a positive correlation between D and $\bar{\mathcal{E}}_{MW}$. However, this correlation weakens for high trainability, as evidenced by the top row. Nine Aadj-M heatmaps provide detailed insights into the connections between each pair of qubits. The heatmaps in the right column exhibit high connection probabilities, signifying the positive correlation between the complex connection structure and high entanglement. A uniformly distributed color represents a equal probability of connection, as depicted in the bottom row, which naturally correlates with low trainability. The heatmaps in the top two rows display high-connection probabilities along the secondary

diagonal with an offset of 1. Consequently, PQCs corresponding to the top two rows are more akin to a nearest-neighbor connection topology, while those in the third row resemble an arbitrarily connected topology.

Algorithm 1: Generating PQCs.

Data: numbers of gates and qubits, L and N ;
 ranges of $\bar{\mathcal{E}}_{\text{MW}}$ and $\mathcal{V}_{\partial_\theta C}$.
Result: PQC with certain values of $\bar{\mathcal{E}}_{\text{MW}}$ & $\mathcal{V}_{\partial_\theta C}$.
 1 ranges of $R_{\text{C-Not}}$ and $D \leftarrow$ ranges of $\bar{\mathcal{E}}_{\text{MW}}$ & $\mathcal{V}_{\partial_\theta C}$;
 2 condition = False;
 3 **while** not condition **do**
 4 PQC \leftarrow L and N ;
 5 $R_{\text{C-Not}}$ and $D \leftarrow$ PQC;
 6 **if** both $R_{\text{C-Not}}$ and D in their ranges **then**
 7 $\bar{\mathcal{E}}_{\text{MW}}|_{\text{predicted}}$ and $\mathcal{V}_{\partial_\theta C}|_{\text{predicted}} \leftarrow$ L-G
 networks;
 8 **if** both $\bar{\mathcal{E}}_{\text{MW}}|_{\text{predicted}}$ and $\mathcal{V}_{\partial_\theta C}|_{\text{predicted}}$ in
 their ranges **then**
 9 condition = True
 10 **end**
 11 **end**
 12 **end**

These findings offer remarkable effectiveness for constructing PQCs. Leveraging $R_{\text{C-Not}}$ and D and considering the trained L-G networks, we can efficiently filter the randomly-generated PQCs to identify those with specific $\bar{\mathcal{E}}_{\text{MW}}$ and $\mathcal{V}_{\partial_\theta C}$, see the pseudocode in Algorithm 1, for

example, the nine PQCs provided in the Supplemental Material [56]. The computational time of Algorithm 1 in identifying the target PQC is merely about one millionth of that associated with the conventional parameter space sampling approach, referred to Fig. 1 and the Supplemental Material [56]. That is, the time efficiency is increased by approximately one million times in searching the required PQC with Algorithm 1.

Conclusion.—In summary, this work firstly demonstrates the potential of the L-G networks for predicting the entanglement and trainability of PQCs. Subsequently, these networks are used to demonstrate the negative correlation between entanglement and trainability, proving that the BP phenomenon is statistical and can be circumvented in computational tasks, even at high levels of entanglement. Furthermore, statistical properties of the three topological parameters of PQCs, i.e., the ratio of C-Not gates, the circuit connectivity density, and the average adjacency matrix, are demonstrated on the 2D space of the entanglement and trainability. Finally, using the statistical properties of the topological parameters and the trained L-G networks, we arrive at the algorithm that can quickly and efficiently generate the PQCs with as-required entanglement and trainability.

Acknowledgement.—This work was supported by the National Natural Science Foundation of China (Nos. 61975005 and 12074037), the Beijing Academy of Quantum Information Science (No.Y18G28), and the Fundamental Research Funds for the Central Universities (No.YWF-22-L-938).

-
- [1] J. Preskill, Quantum Computing in the NISQ era and beyond, *Quantum* **2**, 79 (2018).
 - [2] T. Peng, A. W. Harrow, M. Ozols, and X. Wu, Simulating large quantum circuits on a small quantum computer, *Phys. Rev. Lett.* **125**, 150504 (2020).
 - [3] I. Khait, E. Tham, D. Segal, and A. Brodutch, Variational quantum eigensolvers in the era of distributed quantum computers, (2023), [arXiv:2302.14067 \[quant-ph\]](https://arxiv.org/abs/2302.14067).
 - [4] M. Cerezo, A. Arrasmith, R. Babbush, S. C. Benjamin, S. Endo, K. Fujii, J. R. McClean, K. Mitarai, X. Yuan, L. Cincio, and P. J. Coles, Variational quantum algorithms, *Nat. Rev. Phys.* **3**, 625 (2021).
 - [5] A. Peruzzo, J. McClean, P. Shadbolt, M.-H. Yung, X.-Q. Zhou, P. J. Love, A. Aspuru-Guzik, and J. L. O’Brien, A variational eigenvalue solver on a photonic quantum processor, *Nat. Commun.* **5**, 4213 (2014).
 - [6] P. J. J. O’Malley, R. Babbush, I. D. Kivlichan, J. Romero, J. R. McClean, R. Barends, J. Kelly, P. Roushan, A. Tranter, N. Ding, B. Campbell, Y. Chen, Z. Chen, B. Chiaro, A. Dunsworth, A. G. Fowler, E. Jeffrey, E. Lucero, A. Megrant, J. Y. Mutus, M. Neeley, C. Neill, C. Quintana, D. Sank, A. Vainsencher, J. Wenner, T. C. White, P. V. Coveney, P. J. Love, H. Neven, A. Aspuru-Guzik, and J. M. Martinis, Scalable quantum simulation of molecular energies, *Phys. Rev. X* **6**, 031007 (2016).
 - [7] J. R. McClean, J. Romero, R. Babbush, and A. Aspuru-Guzik, The theory of variational hybrid quantum-classical algorithms, *New J. Phys.* **18**, 023023 (2016).
 - [8] J.-G. Liu, Y.-H. Zhang, Y. Wan, and L. Wang, Variational quantum eigensolver with fewer qubits, *Phys. Rev. Res.* **1**, 023025 (2019).
 - [9] S. McArdle, S. Endo, A. Aspuru-Guzik, S. C. Benjamin, and X. Yuan, Quantum computational chemistry, *Rev. Mod. Phys.* **92**, 015003 (2020).
 - [10] H. R. Grimsley, S. E. Economou, E. Barnes, and N. J. Mayhall, An adaptive variational algorithm for exact molecular simulations on a quantum computer, *Nat. Commun.* **10**, 3007 (2019).
 - [11] Z. Qin, X. Li, Y. Zhou, S. Zhang, R. Li, C. Du, and Z. Xiao, Applicability of measurement-based quantum computation towards physically-driven variational quantum eigensolver, *New J. Phys.* **26**, 073040 (2024).
 - [12] E. Farhi, J. Goldstone, and S. Gutmann, A quantum approximate optimization algorithm, (2014), [arXiv:1411.4028 \[quant-ph\]](https://arxiv.org/abs/1411.4028).
 - [13] S. Hadfield, Z. Wang, B. O’Gorman, E. G. Rieffel, D. Venturelli, and R. Biswas, From the quantum approximate optimization algorithm to a quantum alternating operator ansatz, *Algorithms* **12** (2019).
 - [14] L. Zhou, S.-T. Wang, S. Choi, H. Pichler, and M. D. Lukin, Quantum approximate optimization algorithm: Performance, mechanism, and implementation on near-

- term devices, *Phys. Rev. X* **10**, 021067 (2020).
- [15] J. Biamonte, P. Wittek, N. Pancotti, P. Rebentrost, N. Wiebe, and S. Lloyd, Quantum machine learning, *Nature* **549**, 195 (2017).
- [16] K. Mitarai, M. Negoro, M. Kitagawa, and K. Fujii, Quantum circuit learning, *Phys. Rev. A* **98**, 032309 (2018).
- [17] S. Lloyd and C. Weedbrook, Quantum generative adversarial learning, *Phys. Rev. Lett.* **121**, 040502 (2018).
- [18] X. Wang, B. Qi, Y. Wang, and D. Dong, Entanglement-variational hardware-efficient ansatz for eigensolvers, *Phys. Rev. Appl.* **21**, 034059 (2024).
- [19] S. Zhang, Z. Qin, Y. Zhou, R. Li, C. Du, and Z. Xiao, Single entanglement connection architecture between multi-layer bipartite hardware efficient ansatz, *New J. Phys.* **26**, 073042 (2024).
- [20] R. Li, J. Du, Z. Qin, S. Zhang, C. Du, Y. Zhou, and Z. Xiao, Entanglement structure detection via computer vision, *Phys. Rev. A* **110**, 012448 (2024).
- [21] R. Horodecki, P. Horodecki, M. Horodecki, and K. Horodecki, Quantum entanglement, *Rev. Mod. Phys.* **81**, 865 (2009).
- [22] E. Chitambar and G. Gour, Quantum resource theories, *Rev. Mod. Phys.* **91**, 025001 (2019).
- [23] A. C. Nakhil, T. Quella, and M. Usman, Calibrating the role of entanglement in variational quantum circuits, *Phys. Rev. A* **109**, 032413 (2024).
- [24] P. Díez-Valle, D. Porras, and J. J. García-Ripoll, Quantum variational optimization: The role of entanglement and problem hardness, *Phys. Rev. A* **104**, 062426 (2021).
- [25] T. L. Patti, K. Najafi, X. Gao, and S. F. Yelin, Entanglement devised barren plateau mitigation, *Phys. Rev. Res.* **3**, 033090 (2021).
- [26] E. Farhi, D. Gamarnik, and S. Gutmann, The quantum approximate optimization algorithm needs to see the whole graph: A typical case, (2020), [arXiv:2004.09002](https://arxiv.org/abs/2004.09002) [quant-ph].
- [27] D. Stilck França and R. García-Patrón, Limitations of optimization algorithms on noisy quantum devices, *Nat. Phys.* **17**, 1221 (2021).
- [28] J. F. Gonthier, M. D. Radin, C. Buda, E. J. Duskocil, C. M. Abuan, and J. Romero, Measurements as a roadblock to near-term practical quantum advantage in chemistry: Resource analysis, *Phys. Rev. Res.* **4**, 033154 (2022).
- [29] S. Wang, E. Fontana, M. Cerezo, K. Sharma, A. Sone, L. Cincio, and P. J. Coles, Noise-induced barren plateaus in variational quantum algorithms, *Nat. Commun.* **12**, 6961 (2021).
- [30] G. De Palma, M. Marvian, C. Rouzé, and D. S. França, Limitations of variational quantum algorithms: A quantum optimal transport approach, *PRX Quantum* **4**, 010309 (2023).
- [31] J. Kattemölle and J. van Wezel, Variational quantum eigensolver for the heisenberg antiferromagnet on the kagome lattice, *Phys. Rev. B* **106**, 214429 (2022).
- [32] R. Wiersema, C. Zhou, Y. de Sereville, J. F. Carrasquilla, Y. B. Kim, and H. Yuen, Exploring entanglement and optimization within the hamiltonian variational ansatz, *PRX Quantum* **1**, 020319 (2020).
- [33] M. Dupont, N. Didier, M. J. Hodson, J. E. Moore, and M. J. Reagor, Calibrating the classical hardness of the quantum approximate optimization algorithm, *PRX Quantum* **3**, 040339 (2022).
- [34] M. Dupont, N. Didier, M. J. Hodson, J. E. Moore, and M. J. Reagor, Entanglement perspective on the quantum approximate optimization algorithm, *Phys. Rev. A* **106**, 022423 (2022).
- [35] M. Ballarin, S. Mangini, S. Montangero, C. Macchiavello, and R. Mengoni, Entanglement entropy production in Quantum Neural Networks, *Quantum* **7**, 1023 (2023).
- [36] Y. Chen, L. Zhu, N. J. Mayhall, E. Barnes, and S. E. Economou, How much entanglement do quantum optimization algorithms require?, in *Quantum 2.0 Conference and Exhibition* (Optica Publishing Group, 2022) p. QM4A.2.
- [37] S. Sim, P. D. Johnson, and A. Aspuru-Guzik, Expressibility and entangling capability of parameterized quantum circuits for hybrid quantum-classical algorithms, *Adv. Quantum Technol.* **2**, 1900070 (2019).
- [38] V. Havlíček, A. D. Córcoles, K. Temme, A. W. Harrow, A. Kandala, J. M. Chow, and J. M. Gambetta, Supervised learning with quantum-enhanced feature spaces, *Nature* **567**, 209 (2019).
- [39] M. Schuld, A. Bocharov, K. M. Svore, and N. Wiebe, Circuit-centric quantum classifiers, *Phys. Rev. A* **101**, 10.1103/physreva.101.032308 (2020).
- [40] A. Kandala, A. Mezzacapo, K. Temme, M. Takita, M. Brink, J. M. Chow, and J. M. Gambetta, Hardware-efficient variational quantum eigensolver for small molecules and quantum magnets, *Nature* **549**, 242 (2017).
- [41] A. J. C. Woitzik, P. K. Barkoutsos, F. Wudarski, A. Buchleitner, and I. Tavernelli, Entanglement production and convergence properties of the variational quantum eigensolver, *Phys. Rev. A* **102**, 042402 (2020).
- [42] J. R. McClean, S. Boixo, V. N. Smelyanskiy, R. Babbush, and H. Neven, Barren plateaus in quantum neural network training landscapes, *Nat. Commun.* **9**, 4812 (2018).
- [43] C. Ortiz Marrero, M. Kieferová, and N. Wiebe, Entanglement-induced barren plateaus, *PRX Quantum* **2**, 040316 (2021).
- [44] M. Cerezo, A. Sone, T. Volkoff, L. Cincio, and P. J. Coles, Cost function dependent barren plateaus in shallow parametrized quantum circuits, *Nat. Commun.* **12**, 1791 (2021).
- [45] K. Sharma, M. Cerezo, L. Cincio, and P. J. Coles, Trainability of dissipative perceptron-based quantum neural networks, *Phys. Rev. Lett.* **128**, 180505 (2022).
- [46] M. Cerezo and P. J. Coles, Higher order derivatives of quantum neural networks with barren plateaus, *Quantum Sci. Technol.* **6**, 035006 (2021).
- [47] Z. Holmes, A. Arrasmith, B. Yan, P. J. Coles, A. Albrecht, and A. T. Sornborger, Barren plateaus preclude learning scramblers, *Phys. Rev. Lett.* **126**, 190501 (2021).
- [48] S.-X. Zhang, C.-Y. Hsieh, S. Zhang, and H. Yao, Neural predictor based quantum architecture search, *Mach. Learn.: Sci. Technol.* **2**, 045027 (2021).
- [49] K. Nakaji, L. B. Kristensen, J. A. Campos-Gonzalez-Angulo, M. G. Vakili, H. Huang, M. Bagherimehrab, C. Gorgulla, F. Wong, A. McCaskey, J.-S. Kim, T. Nguyen, P. Rao, and A. Aspuru-Guzik, The generative quantum eigensolver (gqe) and its application for ground state search, (2024), [arXiv:2401.09253](https://arxiv.org/abs/2401.09253) [quant-ph].
- [50] F. Furrutter, G. Muñoz-Gil, and H. J. Briegel, Quantum circuit synthesis with diffusion models, *Nat. Mach. Intell.* **6**, 515 (2024).
- [51] S. Aktar, A. Bärtschi, D. Oyen, S. Eidenbenz, and A.-H. A. Badawy, Graph neural networks for parameter-

- ized quantum circuits expressibility estimation, (2024), arXiv:2405.08100 [quant-ph].
- [52] F. Zhang, J. Li, Z. He, and H. Situ, Transformer for parameterized quantum circuits expressibility prediction, (2024), arXiv:2405.18837 [quant-ph].
- [53] A. W. Harrow and R. A. Low, Random quantum circuits are approximate 2-designs, *Commun. Math. Phys.* **291**, 257 (2009).
- [54] J. M. Renes, R. Blume-Kohout, A. J. Scott, and C. M. Caves, Symmetric informationally complete quantum measurements, *J. Math. Phys.* **45**, 2171 (2004).
- [55] C. Dankert, R. Cleve, J. Emerson, and E. Livine, Exact and approximate unitary 2-designs and their application to fidelity estimation, *Phys. Rev. A* **80**, 012304 (2009).
- [56] See the Supplementary material for some background information for PQCs, details of L-G networks, and nine examples of PQCs generated by Algorithm 1.
- [57] P. J. Huber, Robust estimation of a location parameter, in *Breakthroughs in Statistics: Methodology and Distribution*, edited by S. Kotz and N. L. Johnson (Springer New York, New York, NY, 1992) pp. 492–518.
- [58] J. R. McClean, J. Romero, R. Babbush, and A. Aspuru-Guzik, The theory of variational hybrid quantum-classical algorithms, *New J. Phys.* **18**, 023023 (2016).
- [59] J. Romero, R. Babbush, J. R. McClean, C. Hempel, P. J. Love, and A. Aspuru-Guzik, Strategies for quantum computing molecular energies using the unitary coupled cluster ansatz, *Quantum Sci. Technol.* **4**, 014008 (2018).
- [60] I. D. Kivlichan, J. McClean, N. Wiebe, C. Gidney, A. Aspuru-Guzik, G. K.-L. Chan, and R. Babbush, Quantum simulation of electronic structure with linear depth and connectivity, *Phys. Rev. Lett.* **120**, 110501 (2018).
- [61] P.-L. Dallaire-Demers, J. Romero, L. Veis, S. Sim, and A. Aspuru-Guzik, Low-depth circuit ansatz for preparing correlated fermionic states on a quantum computer, *Quantum Sci. Technol.* **4**, 045005 (2019).
- [62] D. A. Meyer and N. R. Wallach, Global entanglement in multiparticle systems, *J. Math. Phys.* **43**, 4273 (2002).
- [63] R. Somma, G. Ortiz, H. Barnum, E. Knill, and L. Viola, Nature and measure of entanglement in quantum phase transitions, *Phys. Rev. A* **70**, 042311 (2004).
- [64] L. Friedrich and J. Maziero, Avoiding barren plateaus with classical deep neural networks, *Phys. Rev. A* **106**, 042433 (2022).
- [65] E. Grant, L. Wossnig, M. Ostaszewski, and M. Benedetti, An initialization strategy for addressing barren plateaus in parametrized quantum circuits, *Quantum* **3**, 214 (2019).
- [66] T. Volkoff and P. J. Coles, Large gradients via correlation in random parameterized quantum circuits, *Quantum Sci. Technol.* **6**, 025008 (2021).
- [67] G. Verdon, M. Broughton, J. R. McClean, K. J. Sung, R. Babbush, Z. Jiang, H. Neven, and M. Mohseni, Learning to learn with quantum neural networks via classical neural networks, (2019), arXiv:1907.05415 [quant-ph].
- [68] A. Skolik, J. R. McClean, M. Mohseni, P. van der Smagt, and M. Leib, Layerwise learning for quantum neural networks, *Quantum Mach. Intell.* **3**, 5 (2021).

Appendix A: Parameterized Quantum Circuits

1. Output states

PQCs act as a bridge connecting classical and quantum computing [37]. Their output states can be written as

$$|\psi_{\theta}\rangle = U(\theta)|0\rangle^{\otimes n}, \quad (\text{A1})$$

where $U(\theta)$ is a parameterized unitary operator, transforming the N -qubit reference state $|0\rangle^{\otimes n}$ into the output one $|\psi_{\theta}\rangle$. Adjusting the parameters θ leads to different output states.

The choice of PQCs depends on the target tasks and therefore, various ansatz architectures for PQCs are developed [58–61]. The widely used one is the hardware-efficient ansatz (HEA), since it is constructed by gates that can be directly executed on near-term quantum hardware. A typical HEA consists of single-qubit gate layers with tunable parameters and two-qubit gate layers providing entanglement. Its parameterized unitary operator, accordingly, has the form,

$$U(\theta) = \prod_{l=1}^{L_{\text{TWO}}} U_l(\theta_l)W_l, \quad (\text{A2})$$

with

$$U_l(\theta_l) = \bigotimes_{j=1}^N R_{\alpha}(\theta_l^j), \quad (\text{A3})$$

where $R_{\alpha}(\theta_l^j) = e^{-i\theta_l^j\sigma_{\alpha}/2}$ and σ_{α} is the Pauli matrix with $\alpha = x, y, \text{ or } z$. The total number of qubits is denoted by N . W_l represents the operator of the l th unparametrized two-qubit gate, with total number being L_{TWO} .

2. Entangling capabilities

The entangling capability of a PQC is linked to its average ability of creating entanglements and commonly measured by state entanglement. Here, we utilize the sampling average of the Meyer-Wallach (MW) entanglement measure [62] to quantify the entangling capability of a PQC. For the N -qubit system, the MW entanglement, \mathcal{E}_{MW} , is defined as below:

$$\mathcal{E}_{\text{MW}}(|\psi\rangle) \equiv \frac{4}{n} \sum_{i=1}^n \mathcal{D}(\Gamma_i(0)|\psi\rangle, \Gamma_i(1)|\psi\rangle), \quad (\text{A4})$$

where $\Gamma_i(b)$ is a linear mapping that acts on a computational basis with $b \in \{0, 1\}$. That is,

$$\Gamma_i(b)|b_1 \dots b_n\rangle = \delta_{bb_i}|b_1 \dots \overset{\ominus}{b_i} \dots b_n\rangle, \quad (\text{A5})$$

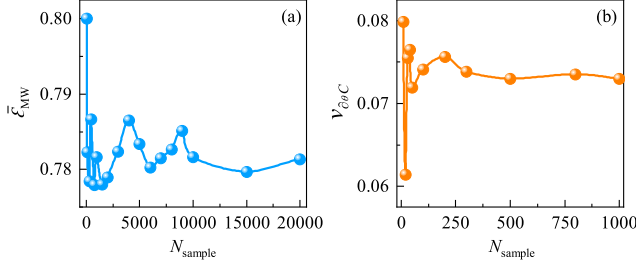


FIG. S1. Statistical variations of the entangling capability $\bar{\mathcal{E}}_{\text{MW}}$ (a) and trainability $\mathcal{V}_{\partial_{\theta} C}$ (b) of the 6-qubit PQCs with the number of samples N_{sample} . As N_{sample} increases, the $\bar{\mathcal{E}}_{\text{MW}}$ and $\mathcal{V}_{\partial_{\theta} C}$ tend to converge and the confidence level increases.

where the symbol \ominus means to remove the i -th qubit. The \mathcal{D} operation is the generalized distance, defined as:

$$\mathcal{D}(|u\rangle, |v\rangle) = \frac{1}{2} \sum_{i,j} |u_i v_j - u_j v_i|^2 \quad (\text{A6})$$

with $|u\rangle = \sum u_i |i\rangle$ and $|v\rangle = \sum v_i |i\rangle$.

As a global measure of multi-particle entanglement for pure states, MW measure has been widely employed as an effective tool in various quantum information applications [62, 63], offering insights into entanglement properties. It is particularly suitable for quantifying the entangling capabilities of PQCs by evaluating their output states [37]. In detail, the entangling capability of a PQC is measured by the average MW entanglement ($\bar{\mathcal{E}}_{\text{MW}}$) among the PQC's output states, sampled in the parameter space of θ , i.e.,

$$\bar{\mathcal{E}}_{\text{MW}} \equiv \frac{1}{|S|} \sum_{\theta_i \in S} \text{MW}(|\psi_{\theta_i}\rangle), \quad (\text{A7})$$

where $S = \{\theta_i\}$ represents the sets of sampled parameter vectors in the parameter space of a PQC and $|S|$ represents the number of sampled parameter vectors. We must sample the parameter space sufficiently to ensure the convergence of $\bar{\mathcal{E}}_{\text{MW}}$ calculated by Eq.(A7). Figure S1(a) indicates that $|S|$ should be on the order of 20 thousands.

3. Trainability

Trainability is an important factor that influences the performance of PQCs. Optimization issues such as the barren plateau (BP) have attracted plenty of attention [64–68]. The so-called BP phenomenon refers to the gradient of a cost function that vanishes exponentially with the system size. We follow the Ref. [42] to measure the trainability of a PQC. Firstly, $U(\theta)$ in Eq. (A2) is separated into the left and right parts,

$$U(\theta) = U_{\mathcal{L}}(\theta)U_{\mathcal{R}}(\theta), \quad (\text{A8})$$

where

$$U_{\mathcal{L}}(\theta) = \prod_{l=k+1}^L U_l(\theta_l)W_l, \quad U_{\mathcal{R}}(\theta) = \prod_{l=1}^k U_l(\theta_l)W_l. \quad (\text{A9})$$

Secondly, the cost function (C) is defined as

$$C = \text{Tr}[HU(\theta)\rho U(\theta)^\dagger], \quad (\text{A10})$$

where H is a Hermitian operator and ρ is an initial state. Thirdly, the gradient of C with respect to θ_k can be written as [42]:

$$\partial_{\theta_k} C \equiv \frac{\partial C(\theta)}{\partial \theta_k} = i\langle 0|U_{\mathcal{R}}^\dagger[V_k, U_{\mathcal{L}}^\dagger H U_{\mathcal{L}}]U_{\mathcal{R}}|0\rangle, \quad (\text{A11})$$

with the Hermitian operator $V_k = \bigotimes_{j=1}^n \sigma_j$. Finally, the variance of $\partial_{\theta_k} C$ is used to measure the trainability, defined as

$$\mathcal{V}_{\partial_{\theta} C} = \langle (\partial_{\theta_k} C)^2 \rangle. \quad (\text{A12})$$

The dynamics of trainability relies on $\mathcal{V}_{\partial_{\theta} C}$, requiring sufficient parameter sampling to obtain stable values. Figure S1(b), where $H = \sigma_1^z \sigma_2^z$ is used, shows that the sampling number is on the order of one thousand.

Model Summary

```

-----
Input:
  Shape: torch.Size([1000, 30, 6, 6])
Reshape:
  Shape: torch.Size([1000, 30, 36])
-----
Layer1: (LSTM)
  l0: Shape: torch.Size([1000, 30, 36])
  l1: Shape: torch.Size([1000, 30, 32])
  l2: Shape: torch.Size([1000, 30, 32])
Layer2: (ReLU)
  Shape: torch.Size([1000, 30, 32])
Layer3: (Dropout)
  Shape: torch.Size([1000, 30, 32])
Layer4: (Reshape)
  Shape: torch.Size([1000, 960])
Layer5: (Linear)
  Shape: torch.Size([1000, 1])
Layer6: (Sigmoid) or (torch.abs)
  Shape: torch.Size([1000, 1])
-----
Output:
  Shape: torch.Size([1000, 1])
-----

```

FIG. S2. Summary of the structure of the L-G network.

Appendix B: L-G networks

1. Structure and dataset

Figure S2 presents the detailed structure of the L-G networks used to predict either $\bar{\mathcal{E}}_{\text{MW}}$ or $\mathcal{V}_{\partial_\theta C}$.

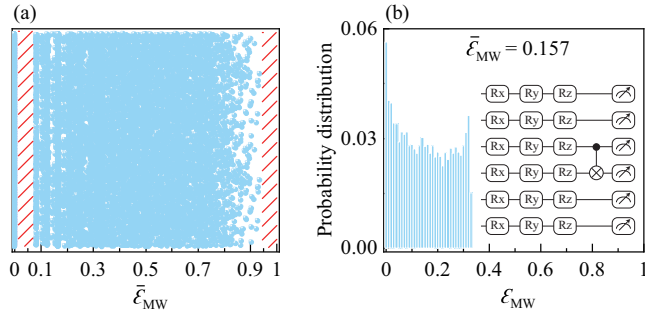


FIG. S3. (a) Distribution of PQC's $\bar{\mathcal{E}}_{\text{MW}}$. There are two gaps near 0 and 1, as indicated by the red diagonal lines. (b) Schematic diagram of calculating $\bar{\mathcal{E}}_{\text{MW}}$ for a PQC with only one C-Not gate using the MW entanglement (\mathcal{E}_{MW}) metric. The inset is the corresponding PQC.

During experiments, we observed that two characteristics for the distribution of $\bar{\mathcal{E}}_{\text{MW}}$. Specifically speaking, there are gaps near 0 and 1, as shown in Fig. S3(a) and Fig. 2(a) of the main text. We would like to clarify that the reason for this does not stem from an inadequate sampling, whereas it is an inherent aspect of the method used to calculate the entangling capability ($\bar{\mathcal{E}}_{\text{MW}}$) of PQCs. We approximate $\bar{\mathcal{E}}_{\text{MW}}$ by sampling the parameter space and calculate the average \mathcal{E}_{MW} among the output states of a PQC. For the PQC without C-Not gate, each output state is a product one, resulting in $\mathcal{E}_{\text{MW}} = 0$ and consequently, $\bar{\mathcal{E}}_{\text{MW}} = 0$. As one C-Not gate is added to the PQC, the output states can take the value of \mathcal{E}_{MW} starting from zero. Therefore, averaging $\bar{\mathcal{E}}_{\text{MW}}$ yields a nonzero $\bar{\mathcal{E}}_{\text{MW}}$, as shown in Fig. S3(b) where $\bar{\mathcal{E}}_{\text{MW}} = 0.157$. Speaking from physics, one C-Not commonly correlates the minimal entanglement and thus the gap of entanglement near zero is due to averaging, similarly for the gap near 1, referred to Fig. S3(a). Note that the minimal non-zero value of $\bar{\mathcal{E}}_{\text{MW}}$ is about 0.08 in Fig. S3(a), larger than 0.157 in Fig. S3(b). This is due to the impact of the C-Not position. The maximum value of $\bar{\mathcal{E}}_{\text{MW}}$ is about 0.92 in Fig. S3(a). Here we also point out that these two types of entanglement gaps would, naturally, diminish as the number of qubits increases.

2. Performance

To encode the circuit structure as input for a machine learning model, a systematic approach is required to represent circuit structures in the form of tensors. The method proposed in [48] involves transforming a circuit

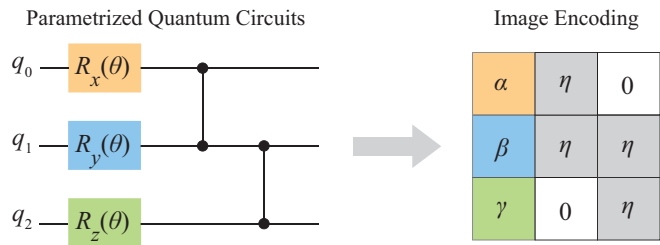


FIG. S4. Image encoding (IE) method for parametrized quantum circuits.

into a multi-channel image encoding (IE), as shown in Fig. S4. The tensor has the shape [depth, qubits, gate types], where the depth corresponds to the number of gate layers. The size of the image is determined by the number of qubits and the circuit's depth. Such an image encoding imposes the following two assumptions on the search space: (a) the two-qubit gates are restricted to act on adjacent qubits and (b) all two-qubit gates symmetrically act on the both qubits. Comparing with the image encoding in Fig. S4, the GTT encoding (Fig. 1 of the main text) does not require these two assumptions and the L-G networks offer at least three merits: (i) the one-gate-to-one-tensor strategy lets the PQCs, containing the same numbers of gates and qubits, possess the mapping third-order tensors with identical size; (ii) the GTT encoding can effectively capture the mutual control information among qubits; (iii) the temporal nature of the LSTM block enables it to simulate the information flow within PQCs.

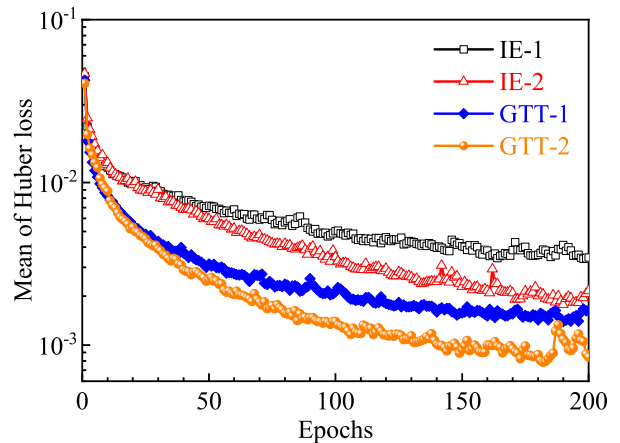


FIG. S5. Variation of learning curves with training epochs for predicting $\bar{\mathcal{E}}_{\text{MW}}$ using image encoding (IE) [48] and gate-to-tensor (GTT) encoding. Each curve represents the mean of Huber loss of ten training processes. Encoding parameters: for number 1, $\alpha = 10$, $\beta = 20$, $\gamma = 30$, and $\eta = 40$; for number 2, $\alpha = 1$, $\beta = 2$, $\gamma = 3$, and $\eta = 4$.

Figure S5 shows the mean of Huber loss of ten repeated experiments on testing dataset as a function of the training epoch. The four cases have the identical net-

work structures except the encoding strategy. Both the GTT encodings outperform both the image encodings [48]. The performance of the GTT encoding depends on the encoding values of α , β , γ , and η . In training, they are taken as the hyper parameters of the L-G network and it is available to take $\alpha = 1$, $\beta = 2$, $\gamma = 3$, and $\eta = 4$ after some experiments.

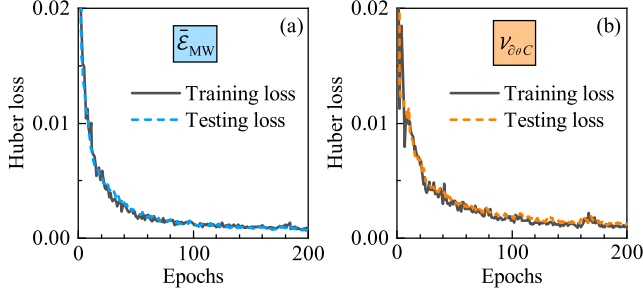


FIG. S6. Variations of Huber losses of the L-G networks for predicting $\bar{\mathcal{E}}_{MW}$ (a) and $\mathcal{V}_{\partial\theta C}$ (b) with the training epochs on the training and testing datasets.

The learning curves of the L-G networks for predicting $\bar{\mathcal{E}}_{MW}$ and $\mathcal{V}_{\partial\theta C}$ are demonstrated by the Huber losses in Fig. S6. Their rapidly downward trends indicate the effectiveness of the L-G networks. The minimal deviation of the Huber losses on the training and testing datasets

suggests the absence of overfitting.

Appendix C: Examples of PQC_s with certain values of $\bar{\mathcal{E}}_{MW}$ and $\mathcal{V}_{\partial\theta C}$

To illustrate the effectiveness of the Algorithm 1 in the main text, we construct a PQC for each square in the nine-square diagram in Fig. 4 of the main text. The generated PQC_s are shown in Fig. S7. The predicted and actual values of $\bar{\mathcal{E}}_{MW}$ and $\mathcal{V}_{\partial\theta C}$ for each PQC validate the accuracy of the algorithm, while the notably short execution time underscores its high efficiency.

Utilizing the conventional parameter space sampling approach with *Pennylane* and *NumPy* libraries, the computation of $\bar{\mathcal{E}}_{MW}$ (sampling 20,000 times) for a single PQC requires approximately 200 seconds and the evaluation of $\mathcal{V}_{\partial\theta C}$ (sampling 1000 times) takes roughly 400 seconds. However, employing the trained L-G networks reduces this time to just a few or tens of milliseconds. By implementing Algorithm 1 multiple times, the number of PQC_s searched before finding the target one is in the thousands, see the search counts in Fig. S7. Accordingly, the conventional sampling approach would necessitate approximately $(200 + 400) \times 1000 \text{ s} \approx 7$ days. Nevertheless, employing Algorithm 1 to search for the PQC requires only several to tens of seconds, as the running time illustrated in Fig. S7. Consequently, the time efficiency is increased by approximately one million times in searching the required PQC with Algorithm 1.

	<p>I</p> $\bar{\mathcal{E}}_{\text{MW}} _{\text{True}}: 0.71$ $\mathcal{V}_{\partial\theta C} _{\text{True}}: 0.45$ Search count: 6619 $\bar{\mathcal{E}}_{\text{MW}} _{\text{Predicted}}: 0.66$ $\mathcal{V}_{\partial\theta C} _{\text{Predicted}}: 0.61$ Runing time: 19.6s
	<p>II</p> $\bar{\mathcal{E}}_{\text{MW}} _{\text{True}}: 0.36$ $\mathcal{V}_{\partial\theta C} _{\text{True}}: 0.81$ Search count: 14184 $\bar{\mathcal{E}}_{\text{MW}} _{\text{Predicted}}: 0.41$ $\mathcal{V}_{\partial\theta C} _{\text{Predicted}}: 0.92$ Runing time: 28.9s
	<p>III</p> $\bar{\mathcal{E}}_{\text{MW}} _{\text{True}}: 0.25$ $\mathcal{V}_{\partial\theta C} _{\text{True}}: 0.71$ Search count: 3754 $\bar{\mathcal{E}}_{\text{MW}} _{\text{Predicted}}: 0.23$ $\mathcal{V}_{\partial\theta C} _{\text{Predicted}}: 0.81$ Runing time: 7.7s
	<p>IV</p> $\bar{\mathcal{E}}_{\text{MW}} _{\text{True}}: 0.65$ $\mathcal{V}_{\partial\theta C} _{\text{True}}: 0.12$ Search count: 677 $\bar{\mathcal{E}}_{\text{MW}} _{\text{Predicted}}: 0.69$ $\mathcal{V}_{\partial\theta C} _{\text{Predicted}}: 0.11$ Runing time: 1.6s
	<p>V</p> $\bar{\mathcal{E}}_{\text{MW}} _{\text{True}}: 0.58$ $\mathcal{V}_{\partial\theta C} _{\text{True}}: 0.13$ Search count: 372 $\bar{\mathcal{E}}_{\text{MW}} _{\text{Predicted}}: 0.57$ $\mathcal{V}_{\partial\theta C} _{\text{Predicted}}: 0.17$ Runing time: 1.0s
	<p>VI</p> $\bar{\mathcal{E}}_{\text{MW}} _{\text{True}}: 0.12$ $\mathcal{V}_{\partial\theta C} _{\text{True}}: 0.11$ Search count: 67 $\bar{\mathcal{E}}_{\text{MW}} _{\text{Predicted}}: 0.13$ $\mathcal{V}_{\partial\theta C} _{\text{Predicted}}: 0.15$ Runing time: 0.4s
	<p>VII</p> $\bar{\mathcal{E}}_{\text{MW}} _{\text{True}}: 0.76$ $\mathcal{V}_{\partial\theta C} _{\text{True}}: 0.05$ Search count: 681 $\bar{\mathcal{E}}_{\text{MW}} _{\text{Predicted}}: 0.71$ $\mathcal{V}_{\partial\theta C} _{\text{Predicted}}: 0.08$ Runing time: 3.0s
	<p>VIII</p> $\bar{\mathcal{E}}_{\text{MW}} _{\text{True}}: 0.61$ $\mathcal{V}_{\partial\theta C} _{\text{True}}: 0.08$ Search count: 1715 $\bar{\mathcal{E}}_{\text{MW}} _{\text{Predicted}}: 0.65$ $\mathcal{V}_{\partial\theta C} _{\text{Predicted}}: 0.09$ Runing time: 5.6s
	<p>IX</p> $\bar{\mathcal{E}}_{\text{MW}} _{\text{True}}: 0.25$ $\mathcal{V}_{\partial\theta C} _{\text{True}}: 0.09$ Search count: 1835 $\bar{\mathcal{E}}_{\text{MW}} _{\text{Predicted}}: 0.29$ $\mathcal{V}_{\partial\theta C} _{\text{Predicted}}: 0.08$ Runing time: 8.1s

FIG. S7. Examples of the PQC's with specific $\bar{\mathcal{E}}_{\text{MW}}$ and $\mathcal{V}_{\partial\theta C}$, drawn using *pennylane*. Each PQC is generated by the Algorithm 1 in the main text, with the corresponding search count for PQC's and running time displayed. The predicted and true values of $\bar{\mathcal{E}}_{\text{MW}}$ and $\mathcal{V}_{\partial\theta C}$ are presented for each PQC.